Supplemental Materials and Methods

Analysis of hormone-responsive genesets

Using our selection criteria for hormone responsive genes, we expect that we are only isolating hormone-dependent genes and not genes that change over developmental time or in culture in a way that is independent of hormonal content. If the expression of a particular gene increases over time (independent of insulin or 20E), for example, we would expect to see its expression at the beginning of the experiment (no culture) be lower than its expression at 4 hrs under all conditions (no hormone, insulin or 20E). This gene would not, however, be identified as hormone responsive, since its expression in culture without hormone must differ from its level in culture with either insulin or 20E.

Nonetheless, it is possible that the progression of time and/or developmental progression could affect differences in expression levels that we observe in the hormone-responsive genesets at 4hr vs 9hr. For example, in Fig 4, we show that some genes have a stronger response to 20E at 9hr than at 4hr. It is possible that over developmental time, the expression of these genes may increase and that this increase over time in culture reflects a natural developmental progression. At the moment we have no way of controlling for these situations, because we only performed the transcriptomics on uncultured discs from animals of one timepoint. As another example, we identified a small group of genes whose expression after 4hr of culture in any condition is different from that of uncultured discs but recovers by 9hr to become closer to uncultured (96hr AEL) levels, both in insulin and in 20E. Because we chose to identify genes that were specific/common to 20E and insulin by comparing genes that were regulated at 9hr by 20E and 4hr by insulin, 11 genes that fit this pattern were falsely identified as being 20E-responsive (responding equally well to insulin or 20E at 9hr but to neither at 4hr). These genes were filtered out of our heatmaps in Fig. 5.

The functional classifications used in Fig. S6 and Fig. 5 are explained as follows: DNA replication/cell cycle includes anything having a positive effect on DNA replication and/or cell cycle progression. Cell death/DNA damage includes genes annotated with a function in apoptosis, programmed cell death, or DNA repair. Protein production includes splicing, translation, ribosome biogenesis, and protein folding. Nutrient transport was limited to proven or predicted members of the SLC/MFS superfamily. The patterning group includes anything known to regulate or be a target of developmental signaling pathways (in any system, not limited to the wing disc). The transcription/chromatin class included verified and putative transcription factors and chromatin modifying proteins. Tissue morphogenesis includes genes involved in cell-cell or cell-ECM contact, as well as cytoskeletal components and regulators. Lastly, the sugar modifications group describes anything involved in protein glycosylation.

Immunofluorescence

Discs were fixed for 20min at room temperature in 4% PFA/PBS. Samples were permeabilized by rinsing twice with PBS+0.1% TritonX100 (TPBS) and blocked with TPBS +0.1mg/ml BSA + 250mM NaCl for 45-60min at room temperature. They were then incubated overnight at 4˚C in primary antibody solution made in PBS+0.1% TritonX100+0.1mg/ml Bovine Serum Albumin (BBX). The next day, stainings were washed in BBX, followed by BBX+4% normal goat serum. Samples were then incubated at room temperature for 2-4hr in the dark with secondary antibodies diluted in BBX. Finally, samples were washed several times in TPBS and mounted between a glass slide and coverglass separated by a double-sided tape spacer. The discs were oriented with their apical surface toward the coverglass and immersed in VectaShield mounting medium (Vector Laboratories H-1000).

Analysis of live imaging

Analysis of cellular contributions to changes in tissue size and shape

The plots of accumulated local tissue shear presented in Fig. 7A and S11 were generated using a Eulerian approach. A fixed grid containing elements of 72 pixels (~14µm) wide was drawn over the tracked tissue region. At each timepoint, cells were assigned to the grid element based on the position of its center. Tissue shear (and its cellular contributions) was calculated from one frame to the next and averaged within each grid element. We then accumulated the average shear contained within each grid element from 2hr (after the adaptation phase) to the end of the movie. For this calculation, we considered only grid elements that have triangles covering more than half of the grid element area at a timepoint.

We quantify the relative area change rate and shear rate, averaged in the tracked wing pouch region, and the corresponding cellular contributions using the Triangle Method (Merkel et al., 2017). The relative area change decomposition states

$$v = \frac{1}{a}\frac{da}{dt} + k_d - k_e,$$

where a is the average cell area and k_d and k_e are cell division and extrusion rates. The relative area change rate v corresponds to the trace of the velocity gradient tensor $\partial_i v_j$. The indices i and j take values x and y. In Fig. 7Bi, we plot the accumulated relative area change of the tracked region of the wing pouch $\int_0^t v\,dt$ (blue line), accumulated relative change of the average cell area $\int_0^t \frac{1}{a}\frac{da}{dt}\,dt$ (green line), accumulated contribution due to cell divisions $\int_0^t k_d\,dt$ (orange line) and the accumulated contribution due to cell extrusions $\int_0^t k_e\,dt$ (cyan line).

The decomposition of the shear rate into its cellular contributions is

$$\tilde{v}_{ij} = \frac{DQ_{ij}}{Dt} + T_{ij} + C_{ij} + E_{ij} + D_{ij}\ ,$$

where Q_{ij} is the cell elongation tensor and D/Dt is a corotational derivative (Merkel et al., 2017). T_{ij}, C_{ij}, E_{ij} and D_{ij} are contributions to the shear rate from T1 transitions, cell divisions, cell extrusions and correlation effects, respectively. In Fig. 7Bii we plot the accumulated xx component of shear of the tracked region $\int_{t_0}^t \tilde{v}_{xx}\,dt$ (blue line), accumulated xx component of shear due to cell elongation change $\int_{t_0}^t \frac{DQ_{xx}}{Dt}\,dt$ (green line), accumulated xx component of shear due to T1 transitions $\int_{t_0}^t T_{xx}\,dt$ (red line), accumulated xx component of shear due to cell divisions $\int_{t_0}^t C_{xx}\,dt$ (orange line), accumulated xx component of shear due to cell extrusions $\int_{t_0}^t E_{xx}\,dt$ (cyan line) and accumulated xx component of shear due to correlation effects $\int_{t_0}^t D_{xx}\,dt$ (magenta line). The x-axis of the coordinate system is parallel to the DV boundary as explained in the main text. The initial timepoint is $t_0 = 2$hr.

The expansion of the wing pouch along the x-axis and the expansion along y-axis perpendicular to it are quantitatively described by velocity gradient components $\partial_x v_x$ and $\partial_y v_y$, respectively. These components of the velocity gradient tensor are determined from v and $\tilde{v}_{xx}$ as

$$\partial_x v_x = \frac{1}{2}v + \tilde{v}_{xx}$$

$$\partial_y v_y = \frac{1}{2}v - \tilde{v}_{xx}\ .$$

We then decompose the velocity gradient components into cellular contributions using the decompositions of v and $\tilde{v}_{xx}$ as follows

$$\partial_x v_x = \left(\frac{1}{2}\frac{1}{a}\frac{da}{dt} + \frac{DQ_{xx}}{Dt}\right) + T_{xx} + \left(\frac{1}{2}k_d + C_{xx}\right) + \left(\frac{1}{2}k_e + E_{xx}\right) + D_{xx}\,,$$

$$\partial_y v_y = \left(\frac{1}{2}\frac{1}{a}\frac{da}{dt} - \frac{DQ_{xx}}{Dt}\right) - T_{xx} + \left(\frac{1}{2}k_d - C_{xx}\right) + \left(\frac{1}{2}k_e - E_{xx}\right) - D_{xx}\,.$$

Here, $\frac{1}{2}\frac{1}{a}\frac{da}{dt} \pm \frac{DQ_{xx}}{Dt}$, $\pm T_{xx}$, $\frac{1}{2}k_d \pm C_{xx}$, $\frac{1}{2}k_e \pm E_{xx}$ and $\pm D_{xx}$ are the contributions to the velocity gradient component from cell shape change, T1 transitions, cell divisions, cell extrusions and correlations, respectively. The upper sign is used in the decomposition of $\partial_x v_x$ and lower sign in the decomposition of $\partial_y v_y$.

In Fig. 7Biii we plot the accumulated wing pouch expansion along the x-axis $\int_{t_0}^{t} \partial_x v_x\, dt$ (blue line), accumulated cell shape expansion along the x-axis $\int_{t_0}^{t} \left(\frac{1}{2}\frac{1}{a}\frac{da}{dt} + \frac{DQ_{xx}}{Dt}\right) dt$ (green line), accumulated contribution to the expansion along the x-axis due to T1 transitions $\int_{t_0}^{t} T_{xx}\, dt$ (red line), accumulated contribution to the expansion along the x-axis due to cell divisions $\int_{t_0}^{t} \left(\frac{1}{2}k_d + C_{xx}\right) dt$ (orange line), accumulated contribution to the expansion along the x-axis due to cell extrusions $\int_{t_0}^{t} \left(\frac{1}{2}k_e + E_{xx}\right) dt$ (cyan line) and accumulated contribution to the expansion along the x-axis due to correlation effects $\int_{t_0}^{t} D_{xx}\, dt$ (magenta line).

In Fig. 7Biv, we plot the accumulated wing pouch expansion along the y-axis $\int_{t_0}^{t} \partial_y v_y\, dt$ (blue line), accumulated cell shape expansion along the y-axis $\int_{t_0}^{t} \left(\frac{1}{2}\frac{1}{a}\frac{da}{dt} - \frac{DQ_{xx}}{Dt}\right) dt$ (green line), accumulated contribution to the expansion along the y-axis due to T1 transitions $\int_{t_0}^{t} -T_{xx} dt$ (red line), accumulated contribution to the expansion along the y-axis due to cell divisions $\int_{t_0}^{t} \left(\frac{1}{2}k_d - C_{xx}\right) dt$ (orange line), accumulated contribution to the expansion along the y-axis due to cell extrusions $\int_{t_0}^{t} \left(\frac{1}{2}k_e - E_{xx}\right) dt$ (cyan line) and accumulated contribution to the expansion along the y-axis due to correlation effects $\int_{t_0}^{t} -D_{xx}\, dt$ (magenta line).

In both Fig. 7Biii and Fig. 7Biv the initial timepoint is $t_0 = 2$hr.

Estimation of tracking errors

Even if the cells are perfectly segmented in each frame of the timelapse, the automated cell tracking can still produce errors in tracking. These errors include false positive and false negative divisions, false positive extrusions and false positive cell appearances. The tracking errors either falsely remove or add a cell to the tissue. Since the overall cell number does not depend on the precision of tracking, the tracking errors always appear in pairs. For example, if a cell track is lost from frame 1 to 2, it is given a new cell ID in frame 2. This one error would cause the counting of a false extrusion (as the cell is thought to be lost in frame 1) and a false cell appearance (to account for the arrival of a new unique track in frame 2). Alternatively, the new cell ID in frame 2 could be attributed to a false cell division, if it is interpreted to be the daughter of a (false) division by a neighboring cell. These pairs of false cell events occur close to each other in space and

time. We use this property to identify the tracking errors and adjust our quantification of the cellular contributions to tissue area change accordingly.

We have never observed any insertion of new cells into the wing disc epithelium and we thus assume that any cell appearance, not associated with a cell division, is due to an error in either segmentation or tracking. We devised a method to independently identify candidates for false positive and false negative divisions using the fact that just before the division, the apical area of the cell increases significantly as the nucleus moves apically. We measure the maximal cell area and the ratio of maximal cell area to the average of the cell area throughout the timelapse for each cell. We then discriminate dividing and non-dividing cells by performing a k-means classification on these two variables (Jones, 2001-). One type of error that could not be identified by this method might occur if the original tracking identifies two cell divisions for the same cell where only one actually occurs. In these situations, when the divisions are separated by less than six frames, we take the later division to be true and the earlier one to be false. Using these candidates for dividing and non-dividing cells we construct a list of candidates for false positive and false negative divisions in the original tracking.

Finally, we pair cell appearances with cell extrusions and false negative cell division candidates, and then we pair the false positive cell division candidates with the remaining cell extrusions and remaining false negative cell division candidates. The cell events we manage to pair in this way we treat as false, and we adjust the cell event counting accordingly.

To construct pairs of these cell events where each event can appear at most once, we introduce a distance measure between cell events A and B in time and space:

$$d(A,B) = \sqrt{\frac{1}{2}(f_A - f_B)^2 + (x_A - x_B)^2 + (y_A - y_B)^2}$$

where $x_{A,B}$and $y_{A,B}$ are coordinates of the cell centers (in pixels) in frame $f_{A,B}$ of the cell event, for each of the two cell events. We then iteratively construct pairs of false cell events from all possible combinations by repeating the following steps:

find a cell event pair with minimum d(A,B)

- if d(A, B) > 25 stop the procedure
- if d(A, B) < 25 identify pair (A, B) as a pair of false cell events
- remove the events A and B from consideration in future iterations

This method identifies more than 90% of the cell appearances as false. It also finds that between 85-90% of cell divisions and 45-75% of cell extrusions initially identified by Tissue Analyzer were true events and that between 10-20% of true divisions were not recognized by Tissue Analyzer. We used the corrected numbers of cell divisions and extrusions to calculate contributions to tissue area change. The remaining number of cell appearances is very low (<10) in all three experiments and not shown in the relative area change plots. This method does not identify the daughter cells. Therefore, in the shear calculation by the Triangle Method, we used the original tracking by the Tissue Analyzer. If we assume that the errors in cell division tracking are not correlated with the cell division orientation and that the falsely identified cell divisions are not oriented on average, we can estimate the relative error of the shear due to cell divisions to be equal to the fraction of true division events not recognized by the Tissue Analyzer i.e. 10-20%.

Figure S1:
Lower 20E concentration does not prevent the arrest of proliferation in insulin

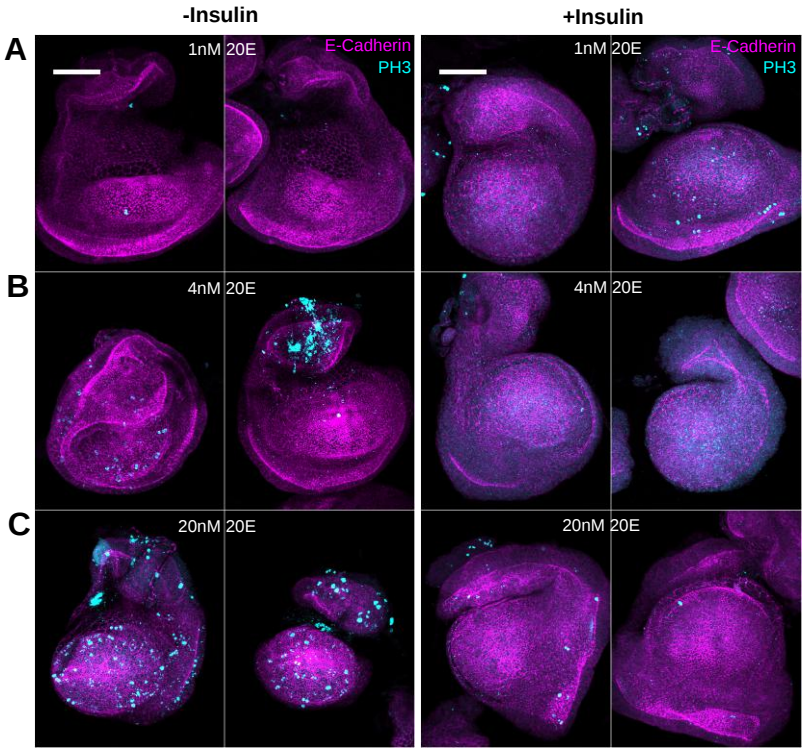

To determine whether lower concentrations of 20E would allow insulin to further improve proliferation, discs were cultured for 24hr in 1nM (A), 4nM (B) or 20nM (C) 20E, with or without 5ug/ml insulin (right/left, respectively). After this length of culture, discs start to lose their morphology, making quantification difficult. In particular in insulin (+/- 20E), the pouch region balloons forward and out. In all discs, the prospective notum starts to curl forward. Only in 20nM 20E alone (without insulin) is there any consistent division remaining. Best attempts were made to orient images with anterior to the left and dorsal up. Scale bar is 50um.

Figure S2:
Cellular component GO terms enriched in subgroups of insulin regulated genes

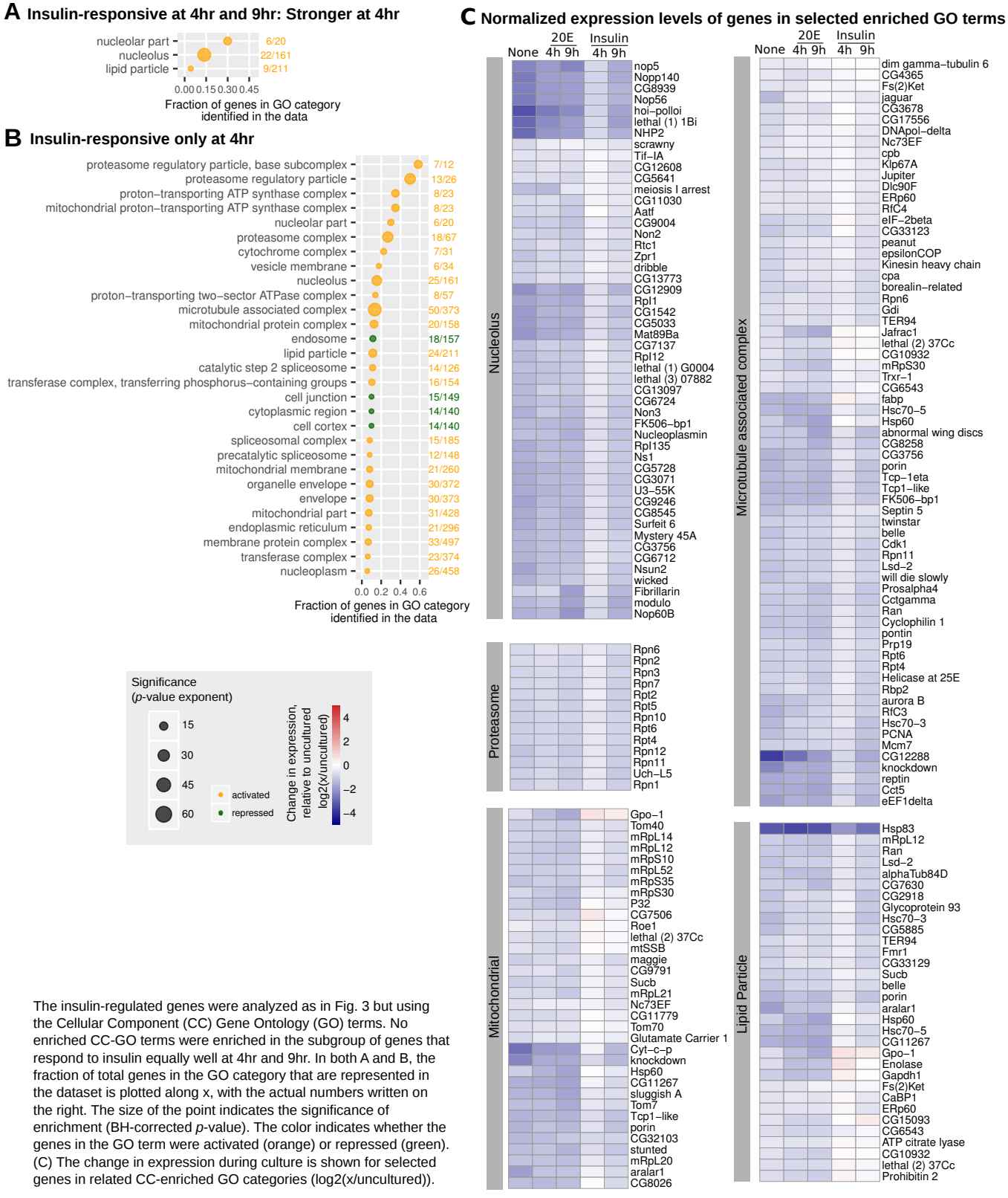

The insulin-regulated genes were analyzed as in Fig. 3 but using the Cellular Component (CC) Gene Ontology (GO) terms. No enriched CC-GO terms were enriched in the subgroup of genes that respond to insulin equally well at 4hr and 9hr. In both A and B, the fraction of total genes in the GO category that are represented in the dataset is plotted along x, with the actual numbers written on the right. The size of the point indicates the significance of enrichment (BH-corrected *p*-value). The color indicates whether the genes in the GO term were activated (orange) or repressed (green). (C) The change in expression during culture is shown for selected genes in related CC-enriched GO categories (log2(x/uncultured)).

Figure S3:
Known targets of TOR and FoxO transiently respond to insulin in cultured wing discs

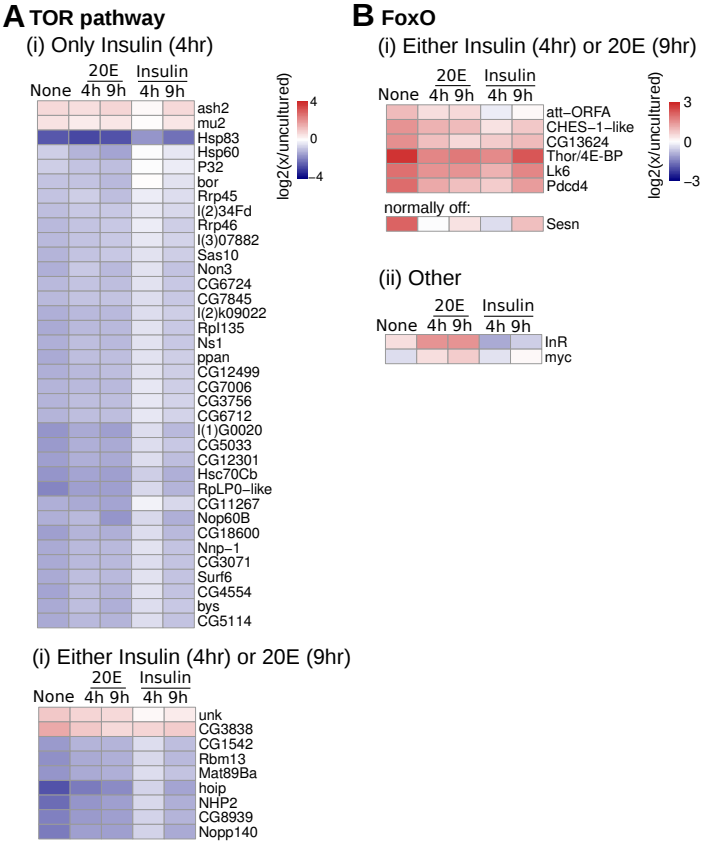

The expression levels of previously-identified TOR- (A) and FoxO-responsive (B) genes were examined in the dataset from wing discs cultured in insulin or 20E. Shown are the changes in expression from that in uncultured discs (log2(x/uncultured)). In (A), genes are grouped based on whether they respond to only insulin (i) or to either insulin or 20E (ii). In (B), most of the FoxO target genes were found to respond to both insulin (at 4hr) and 20E (at 9hr) (i). The *sesn* gene is normally not expressed in wing discs, but becomes upregulated in certain culture conditions. For this case, we report its change in expression relative to our minimum cutoff for expression (5 fpkm). We also show in (ii) values for the insulin receptor (*dInR*) and *myc*, which are thought to be FoxO targets.

Figure S4:
PI3K remains active throughout long term culture in insulin

A **PH-GFP reporter of PI3K activity during culture with insulin alone**

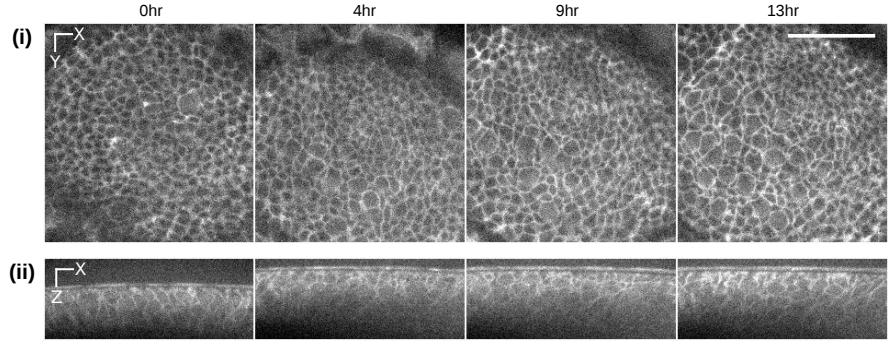

B **PH-GFP reporter of PI3K activity during culture without hormone**

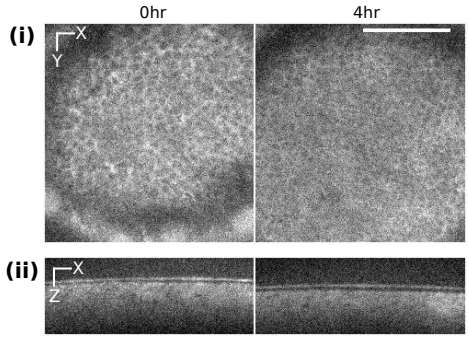

PH-GFP reporter of PI3K activity during culture with insulin (A) or no hormone (B). This reporter localizes to the membrane upon PIP3 production, thus reflecting PI3K activity. A single xy plane is shown in (i) and an xz slice through the middle of the disc is shown in (ii). Timepoints shown in each part are from the same disc grown on the microscope. Scale bar is 20um.

Figure S5:
Insulin causes cytoplasmic retention of FoxO, even after 9hr of culture

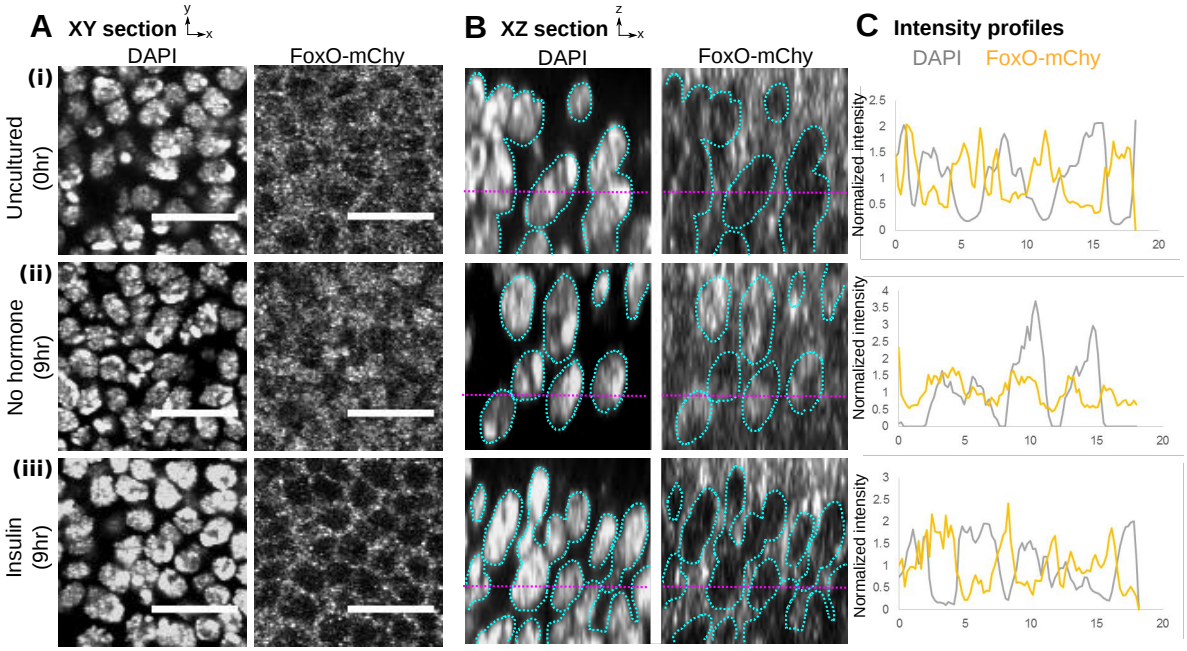

Wing discs from mid-third instar larvae expressing FoxO-mCherry were fixed either immediately after dissection (i) or after 9hr of culture in no hormone (ii) or insulin (iii). They were then stained with DAPI, to mark cell nuclei, and an antibody against mCherry, to mark the FoxO. Shown are single Z-planes (A) or zoomed-in XZ sections (B) from a region of the dorsal-anterior part of the wing pouch. In (B), blue dotted lines trace the outlines of nuclei on both images, and the purple dotted line is the location of the intensity values plotted in (C). In (C), the intensities of DAPI and FoxO-mCherry were normalized for each image to the average intensity of the channel along the line and plotted as a function of position. Scale bars in (A) are 10um.

Figure S6:
Overlap between insulin- and 20E-regulated genesets

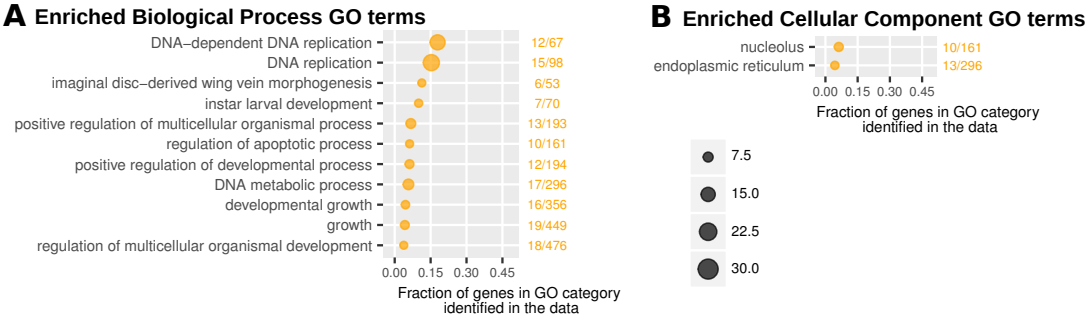

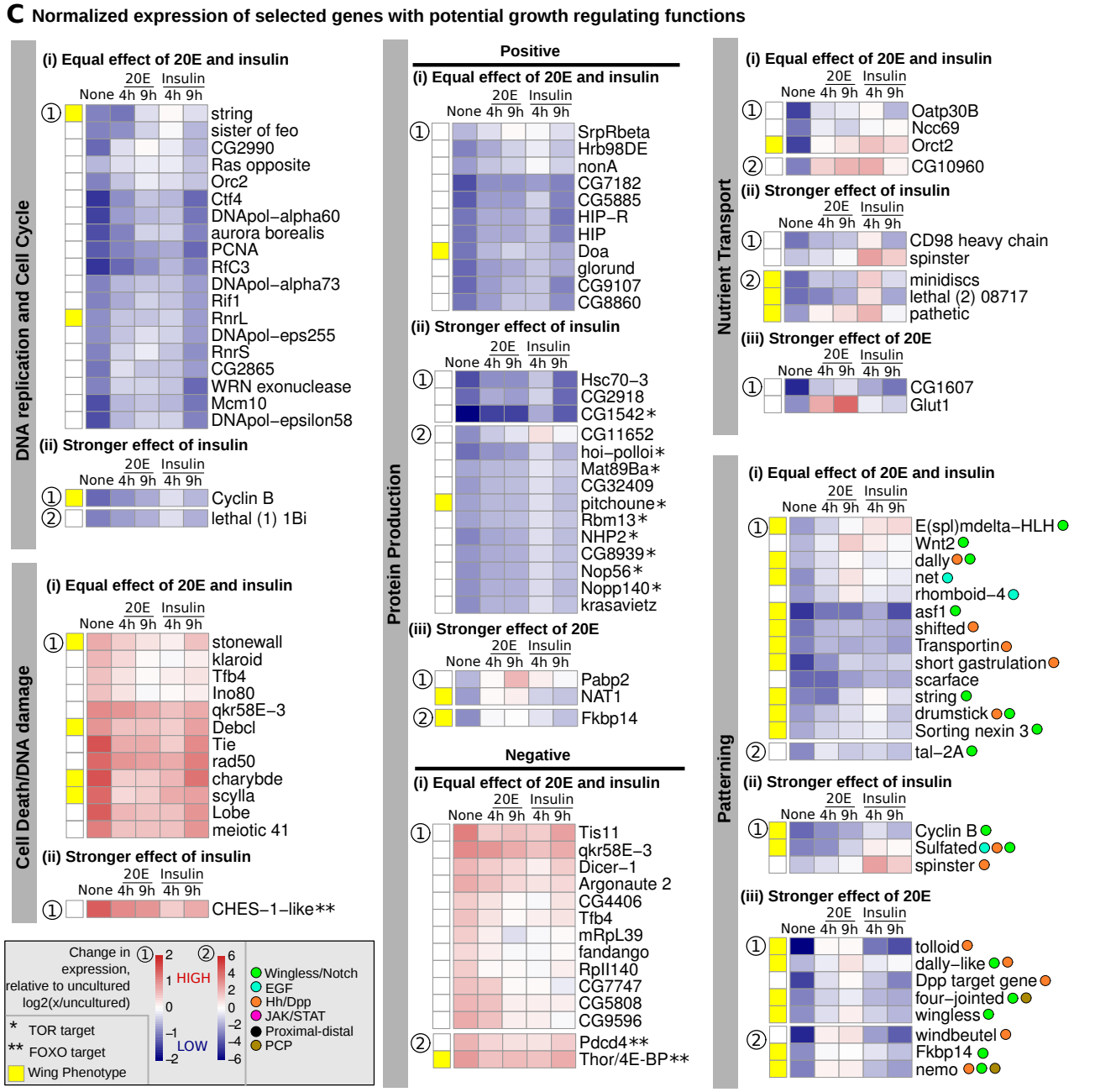

Enriched biological process (A) or cellular component (B) GO terms were identified in the set of genes regulated by both insulin (at 4hr) and 20E (at 9hr). Labels on the right indicate the number of genes in the data over total genes in that GO category. (C) The change in expression from that in uncultured discs (log2(x/uncultured) is shown for genes of selected functional categories. Genes in each group were further subdivided based on whether the two hormones had equal (i) or unequal effects (ii, insulin stronger vs iii, 20E stronger). Genes were plotted on one of two scales (labeled as 1 or 2), depending on how much their values changed across conditions. Yellow squares indicate known phenotypes in the wing (at any stage of development) for loss of function for genes positively regulated by hormone or gain of function for genes negatively regulated by hormone. Asterisks indicate previously identified TOR (*) or FOXO (**) targets.

Figure S7:
20E-signaling is autonomously required for wing growth during the third instar

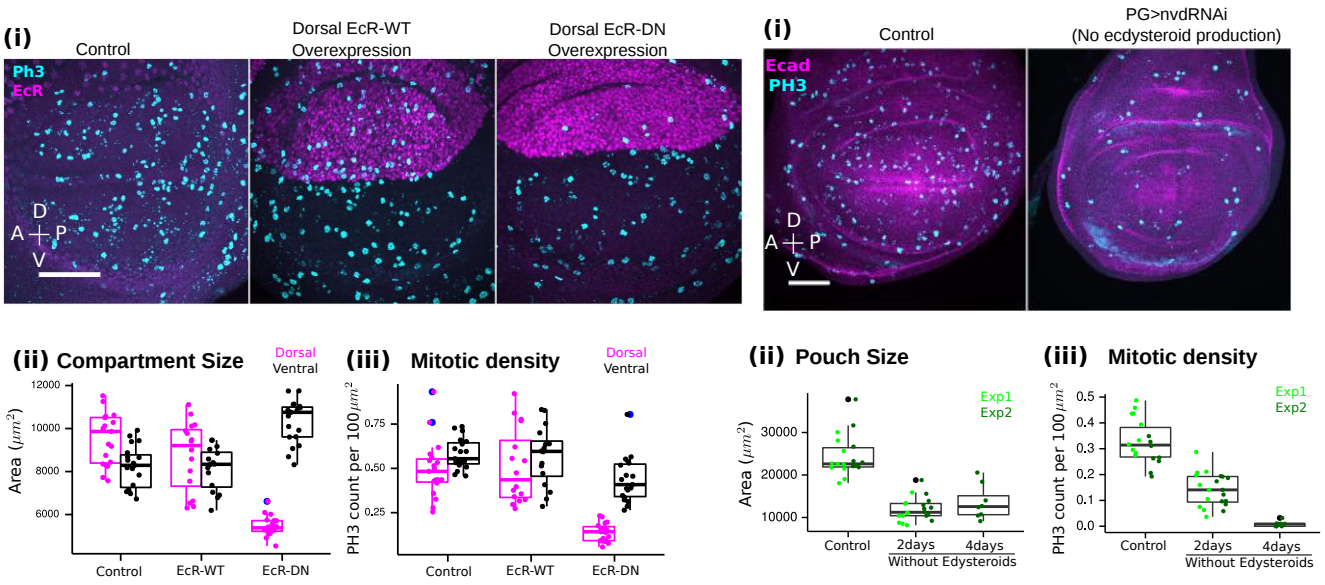

(A) *Apterous-GAL4*, which is expressed in the dorsal compartment of the wing disc, combined with *tub>GAL80ts* was used to overexpress either a wild type (EcR-WT, middle) or dominant negative allele of the Ecdysone Receptor (EcR-DN, right) for 24hr during the third instar. The negative control is the *apterous-GAL4, gal80ts* crossed to wild type (left). (i) Representative images show staining for phospho-Histone-H3 (PH3, a mitotic marker, cyan) as a maximum projection overlaid with EcR (magenta). (ii) Quantification of compartment size (dorsal=pink, ventral=black) was done by measuring area in a maximum projection image. (iii) Mitotic density was measured in the Dorsal (pink) and Ventral (black) compartments by counting number of PH3-positive nuclei per area.

(B) *Phantom-GAL4*, which is expressed in the prothoracic ecdysteroid-producing gland of the brain, combined with *tub>GAL80ts* was used to induce an RNAi targeting neverland (*nvd*) during the third instar. *Neverland* is required to synthesize ecdysteroids. Control larvae, containing only the *phantom-GAL4, tub>GAL80ts* crossed to wild type, formed pupae after 2 days at 29C; *nvd-RNAi* larvae stayed as larvae for several days. (i) Representative images show PH3 staining (cyan) as a maximum projection overlaid with E-cadherin (magenta). Pouch size (area in a maximum projection image, ii) and mitotic density (iii) were measured for the region surrounded by the innermost folds. Data from two independent replicates of the experiment are separately colored.

For both A and B: (i) Scale bar is 50um. In (ii) and (iii), each dot represents one disc, with bars showing the extent of the first and third quartiles; lines reach up to 1.5* IQR (interquartile range); outliers outside of this range are blue (left) or black (right) dots.

Figure S8:
20E-signaling is required in the posterior compartment for Wg expression

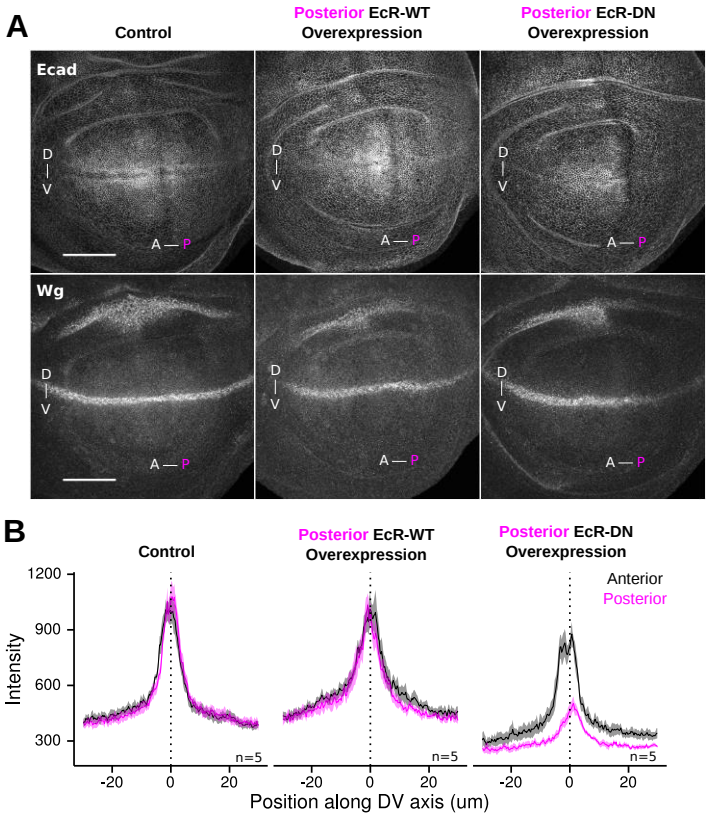

Engrailed-GAL4, which is active in the posterior wing disc, was combined with *tub>GAL80ts* to to transiently overexpress a dominant negative (EcR-DN, right) or wild type (EcR-WT, middle) allele of the Ecdysone Receptor for 24hr in the third instar. The control (left) was *engrailed-GAL4, tub>GAL80ts* crossed to wild type flies. (A) Representative images of E-Cadherin (top) or Wg (bottom) staining in the same discs. Dorsal is up, anterior to the left. Markers deliniate the boundaries. Scale bars are 50um. (B) Wg expression was quantified by measuring the absolute intensity alone a line drawn from Dorsal to Ventral of the pouch in the Anterior (black) or Posterior (pink) compartments. Shown is the mean (dark line) and standard deviation (shaded ribbon) of five discs. Control and perturbation stainings were done in parallel and imaged with the same acquisition settings on the same day.

Figure S9:
Circulating ecdysone is required for wing pattern during growth

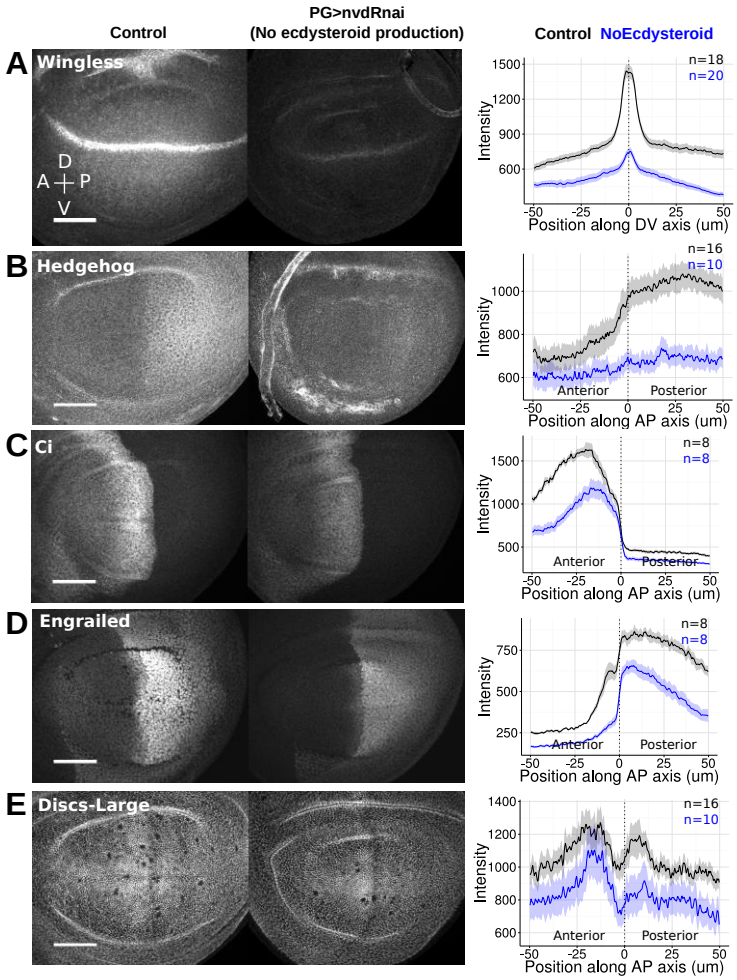

Phantom-GAL4, which is expressed in the prothoracic ecdysteroid-producing gland of the brain, combined with *tub>GAL80TS* was used to induce RNAi against *neverland* (*nvd*), a gene required to synthesize ecdysone, only during the third larval instar. Expression of Wingless (A), Hedgehog (B), Ci, the transcriptional activator downstream of Hh signaling (C), Engrailed, a Hh target gene (D), and Discs-large, a septate junction marker (E) was analyzed by immunofluorescence. Quantification of the changes in expression was performed by plotting the absolute intensity along a line drawn from one compartment to another. For (A), the line was drawn from Dorsal to Ventral in the Anterior comparment. For (B)-(E), the line was drawn from Anterior to Posterior in the Dorsal compartment. Black is the control; blue is the nvd-RNAi animals. The dark line is the mean for all discs measured in the same staining experiment; the shaded ribbon indicates the standard deviation. Control and perturbation stainings were done in parallel and imaged with the same acquisition settings on the same day. Scale bars correspond to 50um.

Figure S10:
Analysis of growth dynamics during live imaging was performed on a fully trackable region of the tissue

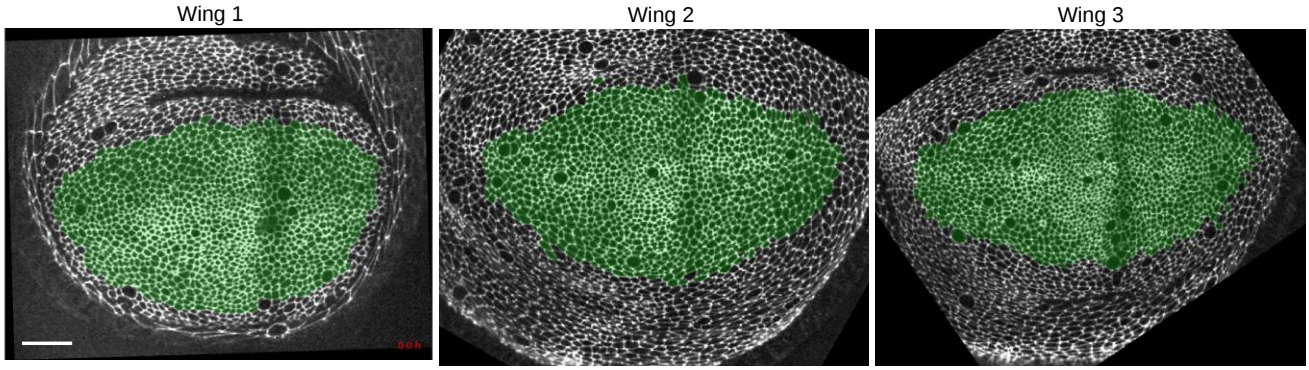

Shown are the first images of each analyzed movie, with green cells highlighting the region that is fully trackable for the length of the timelapse. This region will form the distal wing blade in the adult. Scale bar indicates 20um. Dorsal is up; anterior to the left.

Figure S11:
Patterns of total shear and its cellular contributions measured from live imaging

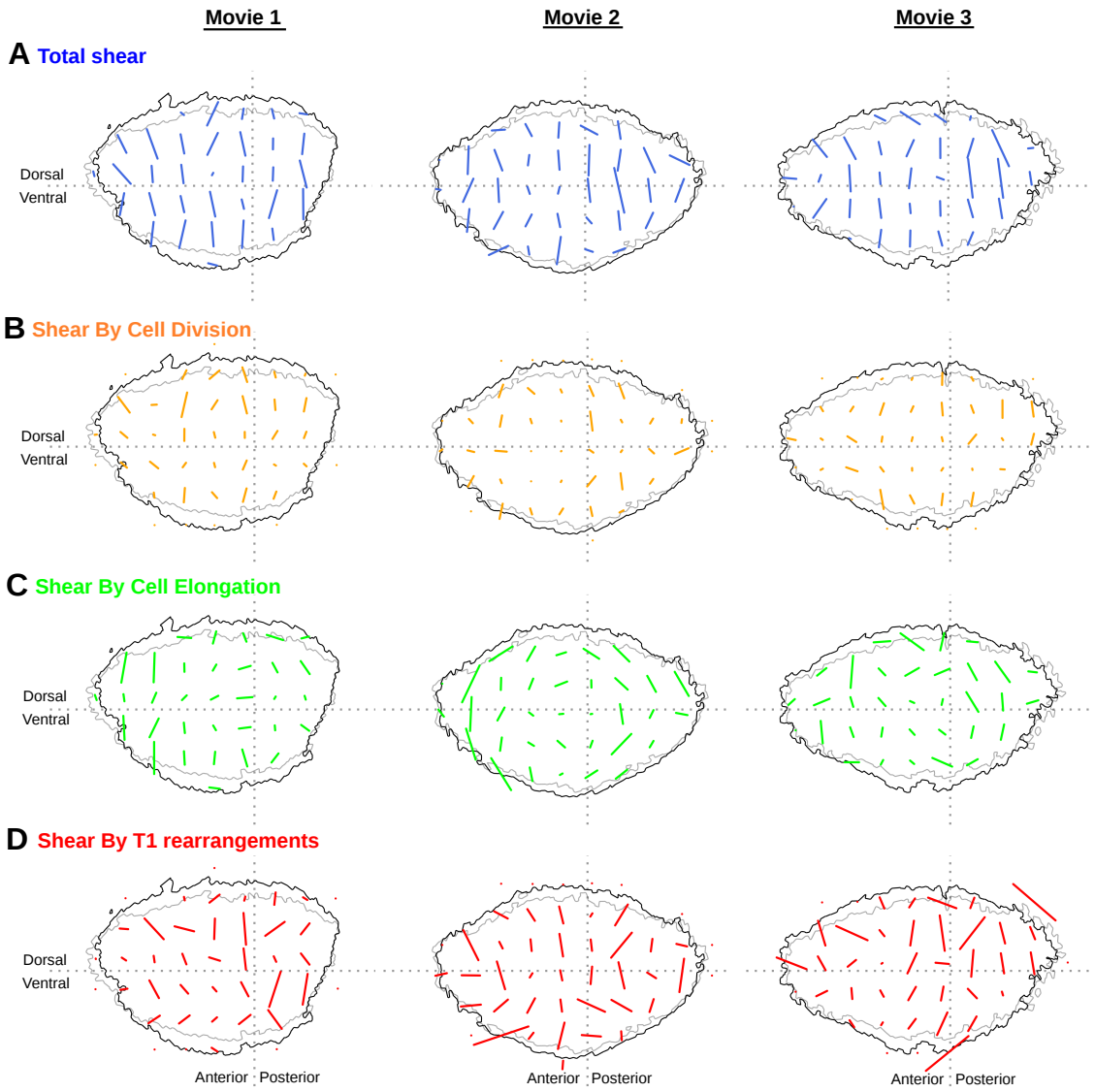

Three E-Cadherin-GFP-expressing wing discs were imaged for >13hr, and cells of the future wing blade region were segmented and tracked. Patterns of tissue shear were measured after the first 2hr adaption phase and are displayed on the outline of the analyzed tissue at the beginning (2hr, grey) and end (13.3hr, black) of the analyzed time window. To generate these shear patterns, we divided the tissue into grid, where each square has a width = 72 pixels. We calculated the area-weighted average tissue shear that occurred between two consecutive frames within each grid and then accumulated this value over time from 2-13hrs. The length of the bar is proportional to its magnitude and its orientation indicates its direction. Shown separately are the patterns for total shear (A, repeated here from Fig. 7A, in order to easily compare to the patterns of cellular contributions), and the contributions to this shear from cell divisions (B), cell elongation change (C), and T1 rearrangements (D).

Supplemental Table S1: List of genes regulated by Insulin at one or both timepoints

Click here to Download Table S1

Supplemental Table S2: List of genes regulated by 20E at one or both timepoints

Click here to Download Table S2

Supplemental Table S3: List of genes regulated at 4hr by insulin alone, 20E alone, or by either hormone

Click here to Download Table S3

Supplemental Table S4: List of genes regulated at 9hr by insulin alone, 20E alone, or by either hormone

Click here to Download Table S4

Supplemental Table S5: List of genes regulated by 4hr in insulin alone, 9hr in 20E alone, or by either hormone at these timepoints

Click here to Download Table S5

Supplemental Movie 1: Long term timelapses of wing discs cultured in 20E

Three E-cadherin-GFP-expressing wing discs were imaged in 20E-containing media, acquiring Z-stacks in a 2x2 tiling every 5 min. Shown are 2D projections of the pseudostratified wing pouch layer after tile stitching. Images were rotated and resized for presentation. Dorsal is up, anterior to the left. Frame rate is 10 frames per second.